Next Materials 8 (2025) 100655

Contents lists available at ScienceDirect

Next Materials

journal homepage: www.sciencedirect.com/journal/next-materials

Research Article

Effect of cations substitution in lead-free double perovskite $Cs_2AgBiBr_6$ solar cells

Nathan Daem [a], Anthony Maho [b], Pierre Colson [a], Gilles Spronck [a], Cédric Malherbe [c], Thi Hieu Hoang [d], Mohamed-Nawfal Ghazzal [d], Guorui He [e], Felix Lang [e], Rudi Cloots [a], Jennifer Dewalque [a,*]

[a] Group of Research in Energy and Environment from Materials (GREEnMat), CESAM Research Unit, Chemistry Department, University of Liège, Allée du Six-Août 13, Liège 4000, Belgium
[b] Université de Bordeaux, CNRS, Bordeaux INP, ICMCB, UMR 5026, 87 Avenue du Docteur Schweitzer, Pessac 33600, France
[c] Mass Spectrometry Laboratory (MSLab), MolSys Research Unit, Chemistry Department, University of Liège, Allée du Six-Août 11, Liège 4000, Belgium
[d] Université Paris-Saclay, UMR8000 CNRS, Institut de Chimie Physique, Orsay 91405, France
[e] ROSI Freigeist Juniorgroup, Physics of Soft Matter, University of Potsdam, Potsdam 14476, Germany

ARTICLE INFO

Keywords:
$Cs_2AgBiBr_6$ double perovskite
Lead-free
Cations substitution
Rubidium
Zinc
Antimony
Thin films
Solar cells
Photovoltaics

ABSTRACT

Cationic substitution can be exploited as strategy to modulate the structural, electronic, and optical properties of perovskite materials. This work investigates the effect of doping $Cs_2AgBiBr_6$ double perovskite compounds as 10 at% Rb, Zn, and Sb-substituted formulations, further incorporated in wet-processed solar cells. Impacts on crystal structure, light harvesting, and charge generation mechanisms are highlighted, especially in terms of photoconversion metrics and efficiency. Regardless of the doping atom, the morphology of the spin-coated photoactive layers presents high homogeneity and coverage rate as well as uniform thickness, matching the characteristics of the undoped benchmark. Advantageously, a significant enhancement of the harvested light is established from UV–VIS spectrometry analyses, with the layers optical band gap notably decreasing from 2.32 to 2.20–2.28 eV following substitution. However, photovoltaic efficiencies calculated from J-V measurements drop from 1.6 % with undoped $Cs_2AgBiBr_6$, to 1.1, 0.3, and 0.4 % with Rb, Zn, and Sb- substituted formulations. Structural analyses of XRD and tolerance factor calculations, combined with Raman and XPS, rationalize these drops by a crystal lattice being too destabilized from the atomic substitutions, especially in Sb- and Zn-substituted samples, with the latest being further undermined by the occurrence of cationic vacancies. Joined UPS, PL and EIS studies also highlight differences of charge transfer properties in the different configurations of solar cells, notably owing to the materials energy levels (mis)alignment. All in all, the present contribution allows for an in-depth understanding of how such cationic substitutions affect $Cs_2AgBiBr_6$ intrinsic behavior and functionality as photovoltaic material, filling a key knowledge gap.

1. Introduction

$Cs_2AgBiBr_6$ double perovskite formulations present tremendous properties for photovoltaic applications. They show high optical absorption coefficients, important chemical stability, and long-lived charge carriers [1–5]. On the other hand, this material is considered to be a promising alternative to lead-containing perovskites, given its low toxicity and long-term resistance to moisture. Nevertheless, its photovoltaic conversion efficiency remains limited to a maximum of 7.9 % due to intrinsic shortcomings [4,6]: notably, its indirect band gap of ~1.8 eV and direct band gap of ~2.2 eV prevent it from efficiently absorbing low-energy photons; its carrier mobility is much lower (~1–12 $cm^2V^{-1}s^{-1}$) than that of lead perovskites (~35 $cm^2V^{-1}s^{-1}$); and the actual carrier lifetimes (about 13.7 ns) is due to numerous defects at the grain boundaries in the $Cs_2AgBiBr_6$ films, acting as dominant non-radiative recombination sites [7]

Therefore, there is a strong need to improve the contemporary efficiencies of $Cs_2AgBiBr_6$-based solar cells by modulating and globally improving the structural, optical, and electronic properties of the double perovskite compounds. An important limitation of $Cs_2AgBiBr_6$ is its

* Corresponding author.
E-mail address: Jennifer.Dewalque@uliege.be (J. Dewalque).

https://doi.org/10.1016/j.nxmate.2025.100655
Received 25 February 2025; Received in revised form 7 April 2025; Accepted 11 April 2025
Available online 21 April 2025

relatively large band gap. A promising approach, which is the subject of this article, is to control the cationic substitutions in its crystal structure, which offers the possibility to manipulate the fundamental characteristics of the material [8–18]. Cationic substitutions allow the incorporation of alternative elements (homovalent and heterovalent) into the crystal structure of the double perovskite, which can lead to significant changes in its physical and chemical properties such as increase absorption at long wavelength, decrease density of defect states, increase theoretical efficiency by decreasing band gap, *etc*. Indeed, the degree of disorder of the (Bi/Ag)Br_6 octahedrons in $Cs_2AgBiBr_6$ strongly affects its electronic band structure, by increasing the number of intrinsic defects that widen the band edges, modify the valence band and conduction band energy levels, and therefore decrease the band gap [4]. Analogous to lead-based perovskites, anion exchange has also been investigated to tune the band gap of the double perovskite compound. In this regard, substituting Br^- by I^- reduces the material's band gap, while the band gap is shifted toward larger values by substituting Br^- with Cl^- [4]. Moreover, it was shown that 1.64 eV band gap value can be achieved by hydrogenation of $Cs_2AgBiBr_6$, resulting from interstitial doping with atomic hydrogen atoms [7]. To determine which cation(s) would be the best to substitute for the different pristine cesium, silver, and bismuth elements in the $Cs_2AgBiBr_6$ double perovskite compound, first, their atomic radii are taken into consideration. Strong deformation of the crystal lattice should be avoided. Therefore, the atoms must have similar atomic radii in similar condition status (*i.e.*, coordination numbers). Rubidium (Rb 172 pm), zinc (74 pm), and antimony (76 pm) are accordingly chosen to replace cesium (188 pm), silver (115 pm), and bismuth (103 pm), respectively [19]. Furthermore, suitable optical properties should be met, for which these substituents have been clearly identified and praised in previous theoretical studies [8,17,20]. However, there are only few experimental studies on the subject [15,16,18]. Notably, Y. Ou *et al.* do not mention in their study the consequences of substituting a monovalent element (Ag^+) by a heterovalent element (Zn^{2+}) [16]. In fact, a Zn^{2+} cation must replace two Ag^+ silver atoms to maintain electroneutrality. This is why cationic silver vacancies are anticipated to occur in the structure. Accordingly, the compound formula is written as $Cs_2(Ag_{1-2x}\square_xZn_x)BiBr_6$ in this work.

In the present study, the effects of substituting these three specific cations are investigated in deep. Specifically, comprehensive analysis is aimed for the substitution of cesium by rubidium ($(Cs_{1-x}Rb_x)_2AgBiBr_6$), silver by zinc ($Cs_2(Ag_{1-2x}\square_xZn_x)BiBr_6$), and bismuth by antimony ($Cs_2Ag(Sb_xBi_{1-x})Br_6$).

From literature, substituting rubidium for cesium is expected to both improve absorption at long wavelengths and reduce the density of defect states, without impacting the crystal lattice. Consequently, the average power conversion efficiency (PCE) of doped devices was reported of nearly 15 % higher than that of standard devices (*i.e.*, 1.39 % vs. 1.21 %), with the champion device reaching 1.52 % with a high fill factor of 78.8 % [18]. Replacing silver with zinc can suppress charge recombination, enhance extraction at the TiO_2/double perovskite interface, reduce the density of defect states in double perovskite materials, and thereby improve the performances of the resulting solar cell [18,21]. The introduction of Zn^{2+} can promote the crystallization of perovskite to develop an excellent surface area and consecutively improve its optical absorbance [16]. Accordingly, the champion efficiency of $Cs_2(Ag_{1-2x}\square_xZn_x)BiBr_6$ (x = 0.10) solar cell increased in comparison with $Cs_2AgBiBr_6$ (2.16 % vs. 1.48 %) [16]. Finally, the substitution of antimony for bismuth led to a reduction in the direct band gap, which improves light absorption properties, and is therefore promising for enhancing photovoltaic performances [15,22]. The best performing $Cs_2Ag(Sb_xBi_{1-x})Br_6$ (x = 0.25) solar cells delivered a slightly increased performance than the reference $Cs_2AgBiBr_6$ (0.30 % vs. 0.20 %).

This study aims at a methodological, step-by-step exploration into the effects of cation substitution on double perovskite compounds – $(Cs_{1-x}Rb_x)_2AgBiBr_6$, $Cs_2(Ag_{1-2x}\square_xZn_x)BiBr_6$ and $Cs_2Ag(Sb_xBi_{1-x})Br_6$ – offering novel insights into the structural tunability of the substituted compounds, correlated to its impact on the light absorption and electronic properties in the double perovskite layer and charge transfer phenomena in the assembled solar cell, which has not yet been established in the literature. By systematically analyzing substitution rates of 5, 10, 15, and 20 at%, this research allows for an in-depth understanding of how such modifications affect the material structural, optical and electronic properties, and its photovoltaic performances, filling a key knowledge gap in the development of efficient lead-free photoactive materials for photovoltaic applications.

2. Experimental section

2.1. Materials and chemicals

Fluorine-doped tin oxide (FTO) covered glass of 2.2 mm thickness and 15 Ω/sq sheet resistance (TEC15, Greatcell Solar Materials) is used as substrates. The following chemicals are obtained from various commercial suppliers, and used without further purification: hydrochloric acid HCl (VWR, 37 %), metallic zinc powder (Roth, ≥98 %), titanium diisopropoxide bis(acetylacetonate) TAA (Sigma-Aldrich, 75 wt% in isopropanol), anhydrous ethanol EtOH (Acros, 99.5 %), TiO_2 nanoparticle paste 18NR-T (Greatcell Solar), titanium chloride $TiCl_4$ (Merck, ≥97.0 %), cesium bromide CsBr (Alfa Aesar, ≥99.9 %), bismuth bromide $BiBr_3$ (Alfa Aesar, ≥99.0 %), silver bromide AgBr (VWR, ≥99.5 %), rubidium bromide RbBr (Sigma-Aldrich, 99.8 %), zinc bromide $ZnBr_2$ (Thermo Scientific, 99.9 %), antimony bromide $SbBr_3$ (Alfa Aesar, 99.5 %), dimethylsulfoxide DMSO (Sigma-Aldrich, >99.9 %), N,N'-dimethylformamide DMF (Acros Organic, 99.9 %), anhydrous chlorobenzene CB (Sigma-Aldrich, 99.8 %), 2,2′,7,7′-Tetrakis[N,N-di(4-methoxyphenyl)amino]-9,9′-spirobifluorene – Spiro-OMeTAD (Borun, >99.9 %), lithium bis(trifluoromethanesulfonyl)imide Li-TFSI (Sigma-Aldrich, 99.95 %), 4-tert-butylpyridine tBP (Sigma-Aldrich, 96 %), anhydrous n-butanol n-BuOH (Fisher, >99.8 %).

2.2. Substrate preparation and deposition of electron transport material

First, FTO glass substrates are cut into 2.0 × 2.0 cm^2 pieces, then etched with HCl (2 M) and metallic zinc powder, so to strip parts of the FTO and prevent short circuits in the final PV cell. Substrates are cleaned over three consecutive washing steps (with soap, ethanol and acetone, respectively) under ultrasonication, before being dried under air. A compact hole blocking layer of TiO_2 (c-TiO_2 ~30 nm thick) is then deposited by ultrasonic spray pyrolysis of TAA (2.2 mL) in ethanol (30.0 mL), from a Sono-Tek ExactaCoat system combined with an AccuMist nozzle. The following spraying parameters are used: stall power of 3.5 W, oxygen carrier gas flow of 0.9 psi, flow rate of 0.25 mL.min^{-1}, nozzle speed of 100 mm.s^{-1}, area spacing of 4 mm, nozzle-to-substrate distance of 5.5 cm, and substrate temperature of 450°C. The deposition pattern is repeated 3 times to obtain a 30 nm thick TiO_2 film. Finally, a thermal treatment at 500°C (ramp 100°C/h) is performed for 30 min, to crystallize TiO_2 in form of anatase phase. After a cleaning treatment under UV-ozone for 15 min, a 150 nm thick mesoporous (mp-) TiO_2 layer is deposited onto the c-TiO_2 layer. Commercial TiO_2 nanoparticle paste (18NR-T, Greatcell Solar Materials) is diluted in absolute ethanol (1:9.8 wt ratio) and spin-coated at 1500 rpm for 30 s, followed by subsequent annealing at 500 °C (with a ramp of 100°C/h) for 30 min. The mp-TiO_2 layer is immersed in an aqueous $TiCl_4$ solution (4.10^{-2} M) for 30 min at 60°C, to allow further improvement of the connectivity between the TiO_2 nanoparticles. Then, samples are successively rinsed with water and EtOH, dried with compressed air, and then calcined for 30 min at 450°C in a preheated oven. Before depositing the $Cs_2AgBiBr_6$-based film, a final cleaning treatment under UV-ozone for 15 min is applied to the samples.

2.3. $Cs_2AgBiBr_6$ double perovskite film preparation

A $Cs_2AgBiBr_6$ solution to produce reference sample is prepared by mixing $BiBr_3$, AgBr and CsBr in 1.0 mL DMSO in an argon-filled glovebox. The preparation of $(Cs_{1-x}Rb_x)_2AgBiBr_6$, $Cs_2(Ag_{1-2x}\square_xZn_x)BiBr_6$ and $Cs_2Ag(Sb_xBi_{1-x})Br_6$ substituted films are respectively prepared by adding RbBr, ZnBr and $SbBr_3$ to the conventional precursors used previously. The masses of precursors and solvent volume used in the synthesis of the different formulations are reported in Table S1.

Solutions are preheated at 75°C to allow the complete dissolution of the precursors. Before spin-coating, both the solution and the substrate are preheated at 75°C. 150 µL of the hot precursor solution is spin-coated onto the mp-TiO_2/c-TiO_2/FTO glass substrates at 2000 RPM for 30 s. The sample is then annealed at 285°C for 5 min under argon atmosphere to allow the formation of the desired double perovskite crystal phase.

2.4. Solar cell fabrication

First, Spiro-OMeTAD (186 mg) and an additive solution (84 µL) are mixed with anhydrous chlorobenzene (2 mL). The additive solution is prepared from 0.175 g Li-TFSI and 312.5 µL of tert-butylpyridine in 1 mL of anhydrous butanol. The solution is then deposited by spin-coating at 2000 RPM for 60 s.

After scratching off the TiO_2/$Cs_2AgBiBr_6$ double perovskite/Spiro-OMeTAD layers from the photoanode contact, a gold counter-electrode layer is deposited by thermal evaporation (home-made apparatus) using a patterned mask.

The resulting photovoltaic device stack is represented by Fig. 1.

2.5. Characterization

A field emission gun microscope TESCAN CLARA, processed under a 15 kV accelerating voltage and high vacuum, is used for the morphological characterization of both individual layers and assembled cells by scanning electron microscopy (SEM). All samples are coated with sputtered gold (10 nm) before characterization.

X-ray diffraction (XRD) was conducted in the fixed θ–2θ geometry on a A Bruker D8 grazing incidence diffractometer instrument using a Cu Kα source ($\lambda = 1.5406$ Å) at a current of 40 A and voltage of 40 V. All references were taken from the PDF4 + database from the International Center for Diffraction Data.

A Shimadzu 3600 Plus instrument with an integrating sphere (ISR-1503) is used for optical measurements by UV–VIS-NIR spectrometry.

X-ray photoemission spectrometry (XPS) analyses are conducted on a Thermo Fisher K-alpha instrument (available by University of Namur, Belgium), equipped with a monochromatic Al Kα source and calibrated with the adventitious carbon (C1s) peak at 285.0 eV. Ultraviolet photoemission spectra (UPS) are acquired using an ESCALB 250 Xi Thermo Fisher instrument (also available by University of Namur, Belgium), equipped with a He lamp (He I-hν = 21.2 eV line) and a six-channeltron detection system, at constant pass energy of 2 eV. To eliminate the contribution of the spectrometer work function, a −10 V bias voltage is applied to the samples. Both XPS and UPS data are processed using the Avantage v.5.9 software (Thermo Fisher Scientific Ltd., UK).

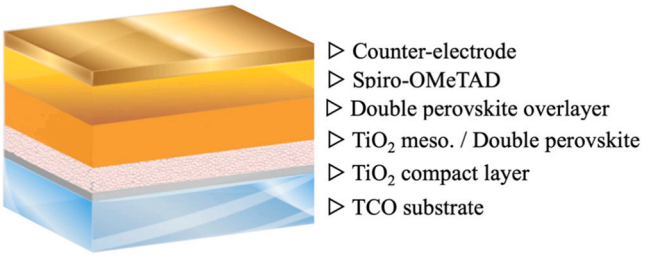

Fig. 1. Scheme of the double perovskite device stack.

Raman spectra are obtained using a benchtop Labram 300 spectrometer (Horiba), interfaced with a 785 nm DPSS laser (maximum input power of 40 mW, applied on the sample) and a thermoelectrically cooled CCD detector Andor iDus DU401 BRDD. The spectrometer is coupled to an Olympus BX40 microscope equipped with a computerized x,y mobile stage. Data are obtained across the 110–1000 cm^{-1} wavenumber offset range with a spectral resolution of ~3 cm^{-1} (grating of 1200 gr/mm). The laser footprint on the sample is ~1 µm in diameter (verified with an Olympus objective X100, NA.80).

Charge carrier lifetime measurements are conducted through time-resolved microwave conductivity (TRMC) measurements, under visible laser excitation (420 nm wavelength) generated with a laser energy of 7.1 mJ cm^{-2}. Analyses are achieved on a nanosecond laser system (EKSPLA), which combines an Nd:YAG laser and an optical parametric oscillator (OPO) that emits 8 ns pulses at adjustable wavelengths ranging from 225 to 2000 nm, with a repetition rate of 10 Hz. For these studies, the probed perovskite layers are uniformly deposited onto glass slides (18 x 18 mm).

Briefly, free excess charge carriers (electrons e^- / holes h^+) induce a relative change in the reflected microwave power ($\Delta P(t)/P$). Eq. 1 below defines the relationship between conductivity and microwave absorption:

$$\frac{\Delta P(t)}{P} = A\Delta\sigma(t) = A\ e\sum\nolimits_i \Delta n_i(t)\ \mu_i \quad (1)$$

Where Δni represents the number of excess charge carriers i at time t, μ_i is the mobility of charge carriers, and A is the time-independent sensitivity factor. A TRMC signal provides information on the maximum intensity value (I_{max}) and on the time decay (I(t)). The maximal intensity of the signal determines the number of created free excess charge carriers upon irradiation, while time decay corresponds to the trapping, recombination, or transfer of charge carriers.

A class A solar simulator (Newport Spectra Physics), coupled to a Keithley 2400 sourcemeter, measures the PV conversion efficiency of the cells (with values averaged over 10 devices). Calibration is performed using a KG5 filtered silicon reference solar cell from Newport. Photocurrent density vs. applied voltage curves (J-V curves) are measured on 2.0 × 2.0 cm^2 devices under simulated 1 SUN illumination (filter AM 1.5) at room temperature, using a black mask with a 0.0355 cm^2 aperture (active area). Forward (0.0–1.2 V) and backward (1.2–0.0 V) measurements are performed with an increment of 4 mV (0.2 s/step).

Electrochemical impedance spectroscopy (EIS) measurements are performed using a BioLogic SP-200 potentiostat (Science Instrument), and collected data are analyzed using the EC-Lab software. A sinusoidal potential perturbation is applied on the assembled devices and the current variation response is recorded. A frequency range of 3 MHz to 85 mHz with 10 mV sinusoidal modulation is applied for data acquisition. Measurements are performed at room temperature under standard 1 sun illumination (AM 1.5 filter) and in open circuit potential (OCP) conditions.

For photoluminescence (PL) measurements, the samples are placed into an integrating sphere (Hamamatsu Photonics K.K. A10094) and illuminated with a 445 nm continuous laser (InsaneWare). An Andor Solis 803 System composed of mirrors and filters is used. A silicon detector with 670 nm center wavelength (CWL) grid is equipped to detect the PL signals, and a filter is used to filter out the signals below 500 nm. The laser intensity is adjusted to 1 sun equivalent intensity according to the specific band gap (2.32 eV) of the absorber, and the intensity is kept the same for all the samples. Photoluminescence quantum yield (PLQY) can be calculated as the ratio of the number of emitted photons to the number of photons absorbed by the samples. The emitted and absorbed photons can be determined by performing the following measurements:

i. Without sample in the integrating sphere, with laser filter for remaining laser correction.
ii. With sample in the integrating sphere, without laser filter for absorptance.
iii. Without sample in the integrating sphere, without laser filter for reference.
iv. With sample in the integrating sphere, with laser filter for emission.

3. Results and discussion

3.1. Morphological, optical and structural properties of double perovskite thin films

Films of $(Cs_{1-x}Rb_x)_2AgBiBr_6$, $Cs_2(Ag_{1-2x}\square_xZn_x)BiBr_6$ and $Cs_2Ag(Bi_{1-x}Sb_x)Br_6$ double perovskites, with $x = 0.00/0.05/0.10/0.15/0.20$, are prepared according the following architecture: FTO-glass/c-TiO_2/mp-TiO_2/double perovskite.

The morphology of the substituted $Cs_2AgBiBr_6$ double perovskite films is evaluated by SEM (Fig. 2 and Figure S1). In general, the higher the substitution ratio, the larger the grain size, with the film appearing as a discontinuous layer of aggregates. Such discontinuity typically hinders charge transfers towards the electron transport layer (ETL),

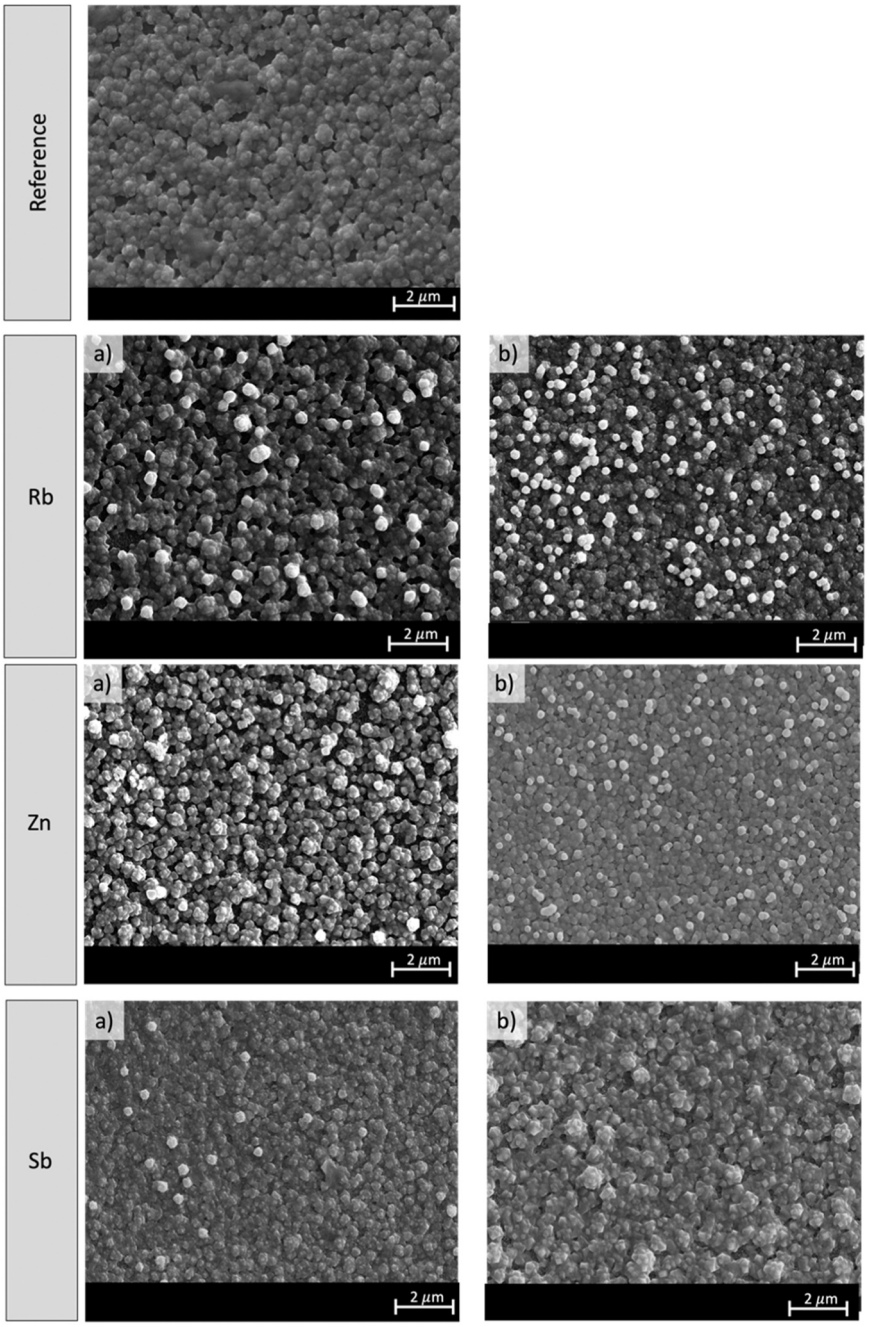

Fig. 2. SEM micrographs of reference $Cs_2AgBiBr_6$ films, and $(Cs_{1-x}Rb_x)_2AgBiBr_6$, $Cs_2(Ag_{1-2x\square x}\ Zn_x)BiBr_6$, and $Cs_2Ag(Bi_{1-x}Sb_x)Br_6$ counterparts, with x = (a) 5 at% and (b) 10 at%.

increases recombination and lowers J_{sc} values in consecutive devices. We have therefore discarded the 15 and 20 at% formulations, henceforth considering only films substituted at 5 and 10 at% for the 3 cationic substitutions, Rb, Zn, and Sb, in addition to the undoped "0 at %" benchmark. Furthermore, literature has shown that, in general, optimal substitutions do not exceed 10 at% due to the formation of impurities such as $Cs_3Bi_2Br_9$ when the substitution rate increases [18]. Focusing thus on the 5 and 10 at%-substituted films (Fig. 2**a,b**), their characteristics appear similar in terms of both morphology (coverage rate and uniformity) and thickness (approximately 200 nm overlayer), as compared to the reference sample. The white aspects observed for some grains is attributed to an artifact from charging effects, occurring on selected crystals being more prominent than their neighbors.

The UV–VIS absorbance spectrum of the spin-coated $Cs_2AgBiBr_6$ reference thin film is reported in Fig. 3**a**. The absorption peak at 350 nm corresponds to the absorption of FTO-glass and TiO_2. Another strong absorption peak is visible at a 440 nm wavelength, as previously observed for $Cs_2AgBiBr_6$ and other double perovskite materials like $Cs_3Bi_2I_9$ [23]. However, the origin of this peak remains unclear [24]. It could be associated to trapped excitonic transitions below the high-energy direct band gap intraband transitions, or to color centers in the material, being defects or imperfections in its crystalline structure [25,26].

Optical spectra of substituted samples (Fig. 3b, c and d) show similar signatures. However, the samples substituted at 10 at% (Rb, Sb and Zn) all absorb more than those substituted at 5 at%. For this reason, only the 10 at%-substituted samples have been considered for further processing into devices. In addition, the overall absorbance of the substituted samples, having the same layer thickness, is greater than that of the reference $Cs_2AgBiBr_6$ sample without substitution. Tauc plots (Fig. 3e) allow for the determination of a reduced band gap for the 10 at %-substituted samples. Indeed, direct band gap values of 2.20, 2.26, and 2.28 eV are respectively measured for Sb, Zn, and Rb 10 %-substituted samples, whereas the band gap value of the reference sample is 2.32 eV. These values are in accordance with the ones previously reported in the literature for similar synthesis conditions [27,28]. The absorbance data highlight the significant potential of cation substitution for modifying the electronic structure and/or for distorting the crystal lattice towards enhanced light absorption.

To investigate the bulk emission properties, the photoluminescence (PL) spectra of the reference and cations substituted films are measured and shown in Fig. 4. PL peaks of the $Cs_2AgBiBr_6$, $(Cs_{1-x}Rb_x)_2AgBiBr_6$, $Cs_2(Ag_{1-2x}\square_xZn_x)BiBr_6$ fall at a similar energy of ~1.9 eV, while the PL peak for $Cs_2Ag(Bi_{1-x}Sb_x)Br_6$ shifts to a lower energy of ~1.8 eV. This is

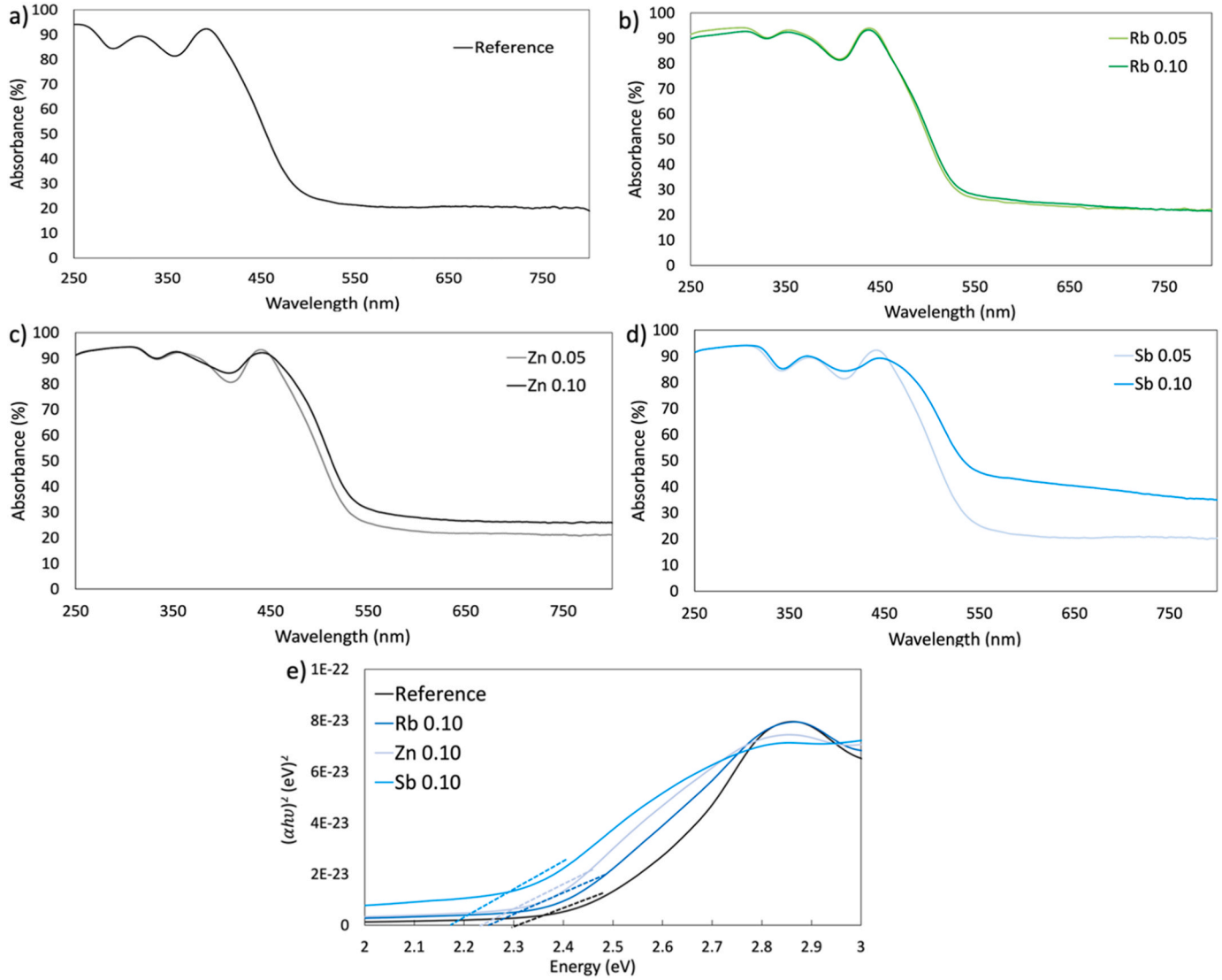

Fig. 3. Absorbance spectra of (a) $Cs_2AgBiBr_6$ (b) $(Cs_{1-x}Rb_x)_2AgBiBr_6$, (c) $Cs_2(Ag_{1-2x\square x}\ Zn_x)BiBr_6$, (d) $Cs_2Ag(Bi_{1-x}Sb_x)Br_6$, with x = 5 at% and 10 at%; (e) Tauc plots (dashed lines: direct band gap estimation) of $(Cs_{1-x}Rb_x)_2AgBiBr_6$, $Cs_2\ (Ag_{1-2x\square x}\ Zn_x)BiBr_6$ and $Cs_2Ag(Bi_{1-x}Sb_x)Br_6$ with x = 10 at%.

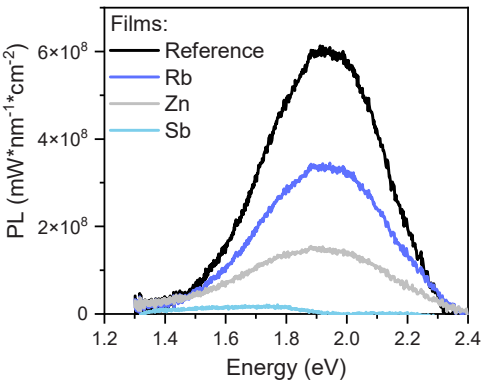

Fig. 4. Photoluminescence spectra of $Cs_2AgBiBr_6$, $(Cs_{1-x}Rb_x)_2AgBiBr_6$, $Cs_2(Ag_{1-2x}\square_x\ Zn_x)BiBr_6$ and $Cs_2Ag(Bi_{1-x}Sb_x)Br_6$ films with x = 10 at% under 1 sun intensity for photoluminescence quantum yield calculation.

consistent with the lowering of the optical band gaps, as shown earlier in the Tauc plots (Fig. 3e). The PL spectra are therefore dominated by recombination across the indirect gap, although recent low-temperature studies suggest that PL emission may arise from color centers in $Cs_2AgBiBr_6$ rather than from band-to-band transitions. The PL peak intensity is higher in the spectrum of the reference film than in those of the substituted ones. An increase in PL intensity is usually attributed to a reduced number of defect sites or to less active defect sites responsible for trap-assisted recombination, showing that cation substitution does indeed impact the electronic structure of the material [5,29].

X-ray diffraction (XRD) analysis are then conducted on all 10 at %-substituted $Cs_2AgBiBr_6$ layers. No secondary phases ($Cs_3Bi_2Br_9$ – with reflections at 12.8° and 30.9°, AgBr – with reflection at 44.2°) are visible in the diffractograms (Figure S2). However, at this stage, there is no evidence of the effective insertion of the cationic substituents in the crystal structure of the double perovskite. Indeed, the diffraction peaks are broad, and the low resolution limits the precise study of the crystal lattice parameters modification that would have been induced by an effective cation substitution, as the errors intrinsic to the measurement method are greater than the structural variations being potentially induced. Furthermore, the cationic substituent is incorporated only in very small quantities, hence the variation on the diffractograms is expected to be too small to be detected. Therefore, basing solely on the diffractograms, the presence of the substituent cannot be confirmed, neither denied, with certainty.

Still, it is crucial to make sure that the substituent cations have been incorporated in the films. Hence, X-Ray photoelectron spectroscopy (XPS) measurements are carried out on $(Cs_{1-x}Rb_x)_2AgBiBr_6$, $Cs_2(Ag_{1-2x}\square_xZn_x)BiBr_6$ and $Cs_2Ag(Bi_{1-x}Sb_x)Br_6$ (with $x = 5$, 10, and 20 at%) samples, as well as on $Cs_2AgBiBr_6$ reference one. This surface-sensitive method, which has not been implemented in the previous literature works on cationic substitutions of $Cs_2AgBiBr_6$ compounds, does confirm here the presence of rubidium (Rb 3d), zinc (Zn 2p) and antimony (Sb 3d) in the considered samples (Figure S3). Further quantification of the presence of the various elements is achieved, focusing the analysis on the substitution of the original cation Cs, Ag, or Bi, by Rb, Zn, or Sb, respectively, and using corresponding high-resolution spectra (Fig. 5).

The different signals (Fig. 5 and Table 1) are then analyzed individually to quantify the substituted elements, based on integrated area values. It should be noted that a peak deconvolution analysis is carried out to discrete the oxygen (O1s around 530 eV) and the antimony peaks, for which changes of intensities in function of Sb doping ratio are difficult to discretely perceive as signals significantly overlap in the same binding energy range. XPS being surface-sensitive, the typical detection depth is generally in the order of a few nm (up to 5 nm) [30]. This is why, according to the measured atomic percentages (Table 1),

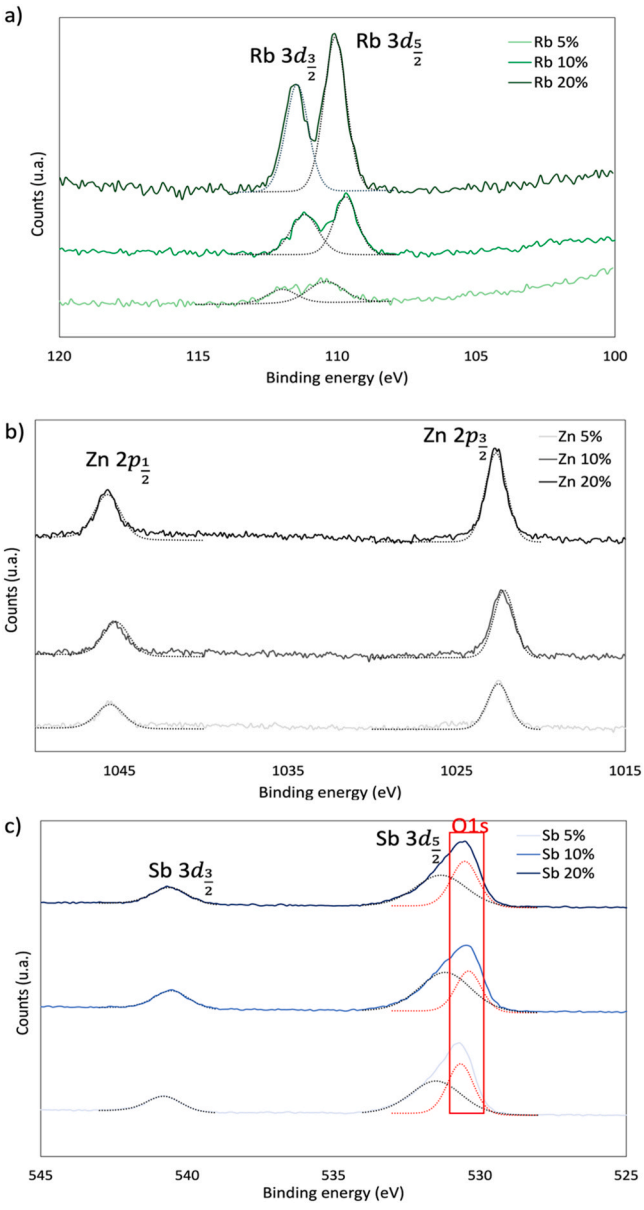

Fig. 5. XPS spectra of (a) $(Cs_{1-x}Rb_x)_2AgBiBr_6$ (Rb 3d), (b) $Cs_2(Ag_{1-2x}\square_x\ Zn_x)BiBr_6$ (Zn 2p) and (c) $Cs_2AgBi_{1-x}Sb_xBr_6$ (Sb 3d) films with x = 5, 10, and 20 at%.

Table 1
Atomic percentage (average value calculated on 3 measurements) determined by XPS from $Cs_2AgBiBr_6$, $(Cs_{1-x}Rb_x)_2AgBiBr_6$ (Rb 3d), $Cs_2(Ag_{1-2x}\square_x\ Zn_x)BiBr_6$ (Zn 2p), and $Cs_2AgSb_xBi_{1-x}Br_6$ (Sb 3d) films, with x = 5, 10, and 20 at%.

	Theoretical atomic percentage (%)	Experimental atomic percentage (%)	σ
Rb	5	4.3	± 0.3
	10	12.3	± 0.6
	20	25.4	± 1.8
Zn	5	34.3	± 1.9
	10	30.1	± 7.3
	20	23.1	± 4.8
Sb	5	6.0	± 0.3
	10	8.3	± 2.5
	20	18.8	± 0.3

variations between theoretical and experimental percentages can be observed. As a representative illustration, the Zn-substituted samples have higher Zn at% values than expected. For zinc, as we substitute Ag

monovalent cation by Zn divalent cation, we can expect the introduction of cationic vacancies. This is why some of the zinc is probably outside the lattice and present in larger quantity at the film surface.

Raman spectroscopy is then considered, in complementarity with XRD and XPS analyses above, for the purpose of phase identification and for probing the effect of substitution in the different samples. Raman spectra of the reference sample (non-substituted $Cs_2AgBiBr_6$ perovskite), and of the 10 at%-substituted (Rb, Zn, and Sb) compounds are presented in Fig. 6a. The Raman spectra of each compound present two bands identified at 134 and 178 cm^{-1}, being respectively attributed to the asymmetric stretching vibration (E_g mode), and to the symmetric stretching vibration ($A_{1\,g}$ mode), of the (Bi/Ag)Br_6 octahedrons. In addition, according to the literature, for Sb substitution level greater than $x = 0.40$, an additional band appears around 206 cm^{-1}, but not for lower ratios [31]. Indeed, Sb is known to hardly substitute Bi beyond a 40 % substitution, except when using mechanochemical or spray-drying synthesis [4]. In consequence, the Raman spectra of the reference, Rb and Sb-substituted (10 % of substitution) samples are similar, and no shift or broadening is observed. However, for the Zn 10 %-substituted sample, the 134 cm^{-1} band is slightly shifted toward higher wavenumbers, highlighting a structural modification in this material formulation.

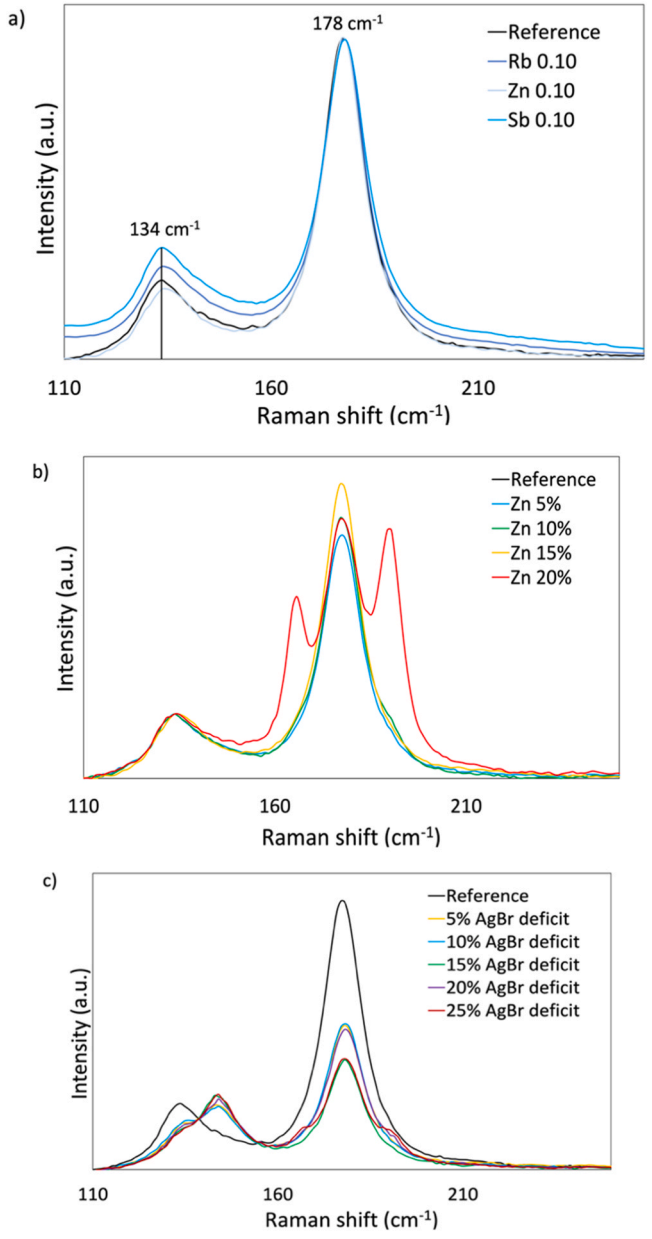

Fig. 6. Raman spectra of (a) $Cs_2AgBiBr_6$, $(Cs_{1-x}Rb_x)_2AgBiBr_6$, $Cs_2(Ag_{1-2x}\square_x\,Zn_x)BiBr_6$, and $Cs_2Ag(Bi_{1-x}Sb_x)Br_6$ films with x = 10 at%; (b) $Cs_2(Ag_{1-2x}\square_x\,Zn_x)BiBr_6$ films with x = 0/5/10/15 and 20 at%.(c) $Cs_2AgBiBr_6$ films with 0(reference)/5/10/15/20 and 25 at% AgBr deficit in precursor solutions (CsBr, AgBr and $BiBr_3$ in DMSO).

To the best of our knowledge, no information is provided in literature to explain this peculiar behavior for the Zn-substituted sample. Knowing that the electroneutrality is not preserved for Ag substitutions by Zn, Raman analysis is conducted for the whole range of substitution rates, *i.e.* 5, 10, 15 and 20 at% (Fig. 6b). A sudden change in the Raman spectra occurs for the 20 at% sample, with two new bands appearing at 165 and 190 cm^{-1} that are assigned to the vibrations of the Bi-Br bonds into the distorted octahedrons in the $Cs_3Bi_2Br_9$ compound. The presence of both zinc atoms and cationic vacancies at the B-sites of the $Cs_2AgBiBr_6$ compound introduces structural instability, leading to a phase transformation toward the non-stoichiometric $Cs_3Bi_2Br_9$ compound. Both materials, $Cs_2AgBiBr_6$ and $Cs_3Bi_2Br_9$ compounds, are then coexisting into the deposited film.

In order to compare the influence of the zinc atoms with respect to the presence of cationic vacancies on the structural stability of the $Cs_2AgBiBr_6$ compound, Ag deficient materials are synthetized under the same experimental conditions – therefore not containing any Zn substituent. Raman spectra are reported in Fig. 6**c**. By increasing Ag deficit (from 5 to 25 at%) and therefore inducing cationic vacancies at the B-sites, that should compensate for electroneutrality by converting some Bi^{3+} cations into Bi^{5+} ones, a strong change occurs in the vibrational behavior of the (Bi/Ag)-Br bonds. Again, we notice that the partial oxidation from Bi^{3+} to Bi^{5+} can induce local distortion of the octahedrons, the ionic radius of Bi^{5+} being of 0.76 Å vs. 1.03 Å for Bi^{3+}. The effect of the cationic substitution on the crystal lattice stability is specifically addressed in Section 3.3. Two bands occur at 134 and 145 cm^{-1}, probably due to the contribution of both Bi^{3+} and Bi^{5+} ions to the stretching vibrations of (Bi/Ag)-Br bonds. A decrease in the intensity of the 178 cm^{-1} band, assigned to the symmetric stretching of the Bi/Ag atoms around the Br atoms, also occurs probably due to the progressive loss of ordering into the structure with increased Ag deficit. For the 25 at % silver deficit, again, the bands at 165 and 190 cm^{-1} (assigned to the vibrations of the Bi-Br bonds into the distorted octahedrons in the $Cs_3Bi_2Br_9$ compound) appear, which indicates a partial phase transformation from $Cs_2AgBiBr_6$ into $Cs_3Bi_2Br_9$, due to structural instability.

All in all, we are thus able to confirm the presence of Rb, Zn, and Sb in the different samples. However, none of the studied techniques formally prove the substitution itself, *i.e.* the presence of the substituent within the lattice, replacing the targeted cationic element.

3.2. Devices assembly and charge properties characterization

The films are then used for further assembly into solar cells, with the following configuration: glass/FTO/c-TiO_2/mp–TiO_2/lead-free double perovskite/Spiro-OMeTAD/Au (Fig. 1), to evaluate photoconversion metrics and efficiencies.

The PV performances of the $Cs_2AgBiBr_6$, $(Cs_{1-x}Rb_x)_2AgBiBr_6$, $Cs_2(Ag_{1-2x}\square_xZn_x)BiBr_6$, $Cs_2Ag(Bi_{1-x}Sb_x)Br_6$ films ($x = 10$ at% in each case) are shown in Fig. 7 and Table 2. Globally, the substitutions lead to a drop of the photovoltaic performances. Indeed, PCE values fall quite significantly for the substituted samples as opposed to the reference one (1.6 %), even more for the Zn (0.4 %) and Sb substitutions (0.3 %) than for the Rb-substituted sample (1.1 %).

To rationalize the evolution of the V_{oc} values of the different samples, the photoluminescence quantum yields (PLQYs) of the $Cs_2AgBiBr_6$, $(Cs_{1-x}Rb_x)_2AgBiBr_6$, $Cs_2(Ag_{1-2x}\square_xZn_x)BiBr_6$ and $Cs_2Ag(Bi_{1-x}Sb_x)Br_6$ films ($x = 10$ at% in each case) were calculated from the PL spectra (**Note S1**). Decreasing PLQY values are observed for the $Cs_2AgBiBr_6$, $(Cs_{1-x}Rb_x)_2AgBiBr_6$, $Cs_2(Ag_{1-2x}\square_xZn_x)BiBr_6$ and $Cs_2Ag(Bi_{1-x}Sb_x)Br_6$ films

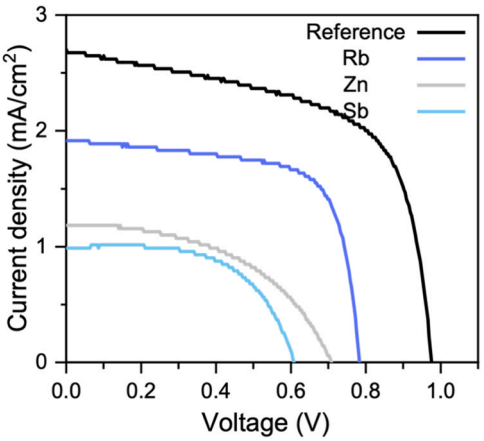

Fig. 7. J-V curves of champion $Cs_2AgBiBr_6$, $(Cs_{1-x}Rb_x)_2AgBiBr_6$, $Cs_2(Ag_{1-2x}\square_x Zn_x)BiBr_6$, and $Cs_2Ag(Bi_{1-x}Sb_x)Br_6$ devices, with x = 10 at%.

Table 2
Photovoltaic parameters of champion $Cs_2AgBiBr_6$, $(Cs_{1-x}Rb_x)_2AgBiBr_6$, $Cs_2(Ag_{1-2x}\square_x Zn_x)BiBr_6$, and $Cs_2Ag(Bi_{1-x}Sb_x)Br_6$ devices, with x = 10 at%.

	V_{oc} (V)	J_{sc} (mA/cm^2)	FF (%)	PCE (%)	PCE (%)
Reference	0.976	2.7	61	1.6	1.5 ± 0.1
Rb	0.784	1.9	69	1.1	1.0 ± 0.2
Zn	0.707	1.2	49	0.4	0.2 ± 0.1
Sb	0.608	1.0	59	0.3	0.2 ± 0.2

($x = 10$ at% in each case), from 0.1 % over 0.06 %, 0.03–0.009 %, see Figure S4a. This suggests increased non-radiative recombination and corresponds well to the trend observed for solar cell performance and V_{OC}. Since the PL emission originated from a weak indirect band gap transition with lower energy compared to the dominating direct band gap [32], relative quasi-Fermi-level splitting changes (ΔQFLS) were analyzed only. As shown in Figure S4b, this analysis suggests a direct correlation of ΔQFLS and ΔVoc for the substituted samples, with a decrease in V_{OC} and QFLS (Table S2) stemming from increased non-radiative recombination with cation substitution.

Electrochemical impedance spectroscopy (EIS) analyses are further conducted on the different $Cs_2AgBiBr_6$-based solar cells, and the corresponding results are presented as Nyquist plots in Fig. 8. Data are fitted with the equivalent circuit model shown in the inset of Fig. 8, and are summarized in Table 3. [5,33–36]

The equivalent electrical circuit consists of: a R_1 resistance associated with wires and contacts (high frequency); a $R_2//Q_2$ element (with Q as constant phase element modelling an imperfect capacitor) characteristic of the selective contacts, including c-TiO_2 and mp-TiO_2 for electron-selective contact and Spiro-OMeTAD for hole-selective contact respectively (medium frequency); and a $R_3//Q_3$ element for interfacial recombination between electrons and holes (low frequency).

The R_2 selective contacts resistance is observed as slightly higher for substituted samples (300, 300, 330 Ω for 10 at%-Rb, Zn, Sb containing materials, vs. 200 Ω for $Cs_2AgBiBr_6$ reference), corresponding to less efficient charge transfer to the selective contacts for these devices, and rationalizing the lower J_{sc} values obtained by J-V measurements (1.9, 1.2, and 1.0 mA/cm^2 for 10 at%- Rb, Zn, and Sb formulations, respectively, vs. 2.7 mA/cm^2 for the $Cs_2AgBiBr_6$ reference).

Regarding R_3, a high value is usually considered as beneficial as the recombination rate at the TiO_2/double perovskite and double perovskite/Spiro-OMeTAD interfaces is inversely proportional to R_3, so it reveals lower interfacial recombination in higher R_3 value-device. However, a much higher Q_3 value is observed for the 10 at%-Rb, Zn, and Sb devices than for the reference one, which means a high accumulation of charges at the interfaces. This trend is not beneficial for PV devices, as blocked charges do not contribute to PV efficiency. Therefore, the reference device allows a globally better charge transfer, and EIS corroborates PV parameters.

These results provide a first step towards explaining the efficiency trend. Obviously, it needs to be consolidated with complementary characterizations.

Accordingly, the effect of cationic substitution is further evaluated regarding the charge carrier lifetime of the double perovskite formulation, thanks to time-resolved microwave conductivity (TRMC) measurements. These are not conducted on fully-assembled devices, well on thin glass samples coated with the perovskite material. The TRMC signal intensity, following laser excitation (420 nm), directly translates the photogenerated free electrons and holes (Figure S5) [37]. Then the free charges face recombination, charge trapping, and surface reaction, which explains the observed decay lifetime [38].

The TRMC signal for the reference sample exhibits the shortest charge lifetime, as shown in Table 4. As the substitution operates, the photogenerated charge carrier lifetime increases, reaching its maximal value for Zn-substituted sample (Table 4). These results are awaited, as a reduced band gap extends charge carrier lifetime [39]. Other parameters such as trap states or exciton binding energy can also influence charge lifetime. So, the substitution of Rb, Zn, and Sb reduces the band gap compared with reference (2.28, 2.26, and 2.20 eV, respectively, *vs.*

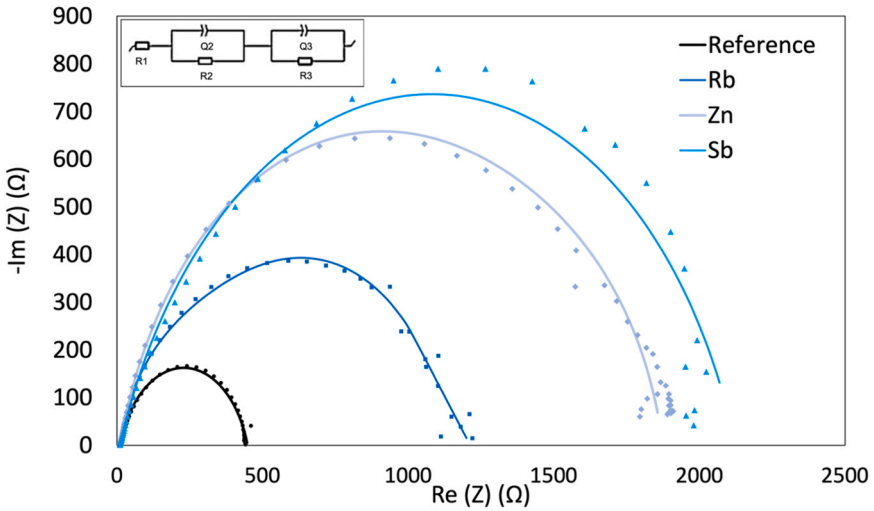

Fig. 8. EIS Nyquist plots of $Cs_2AgBiBr_6$, $(Cs_{1-x}Rb_x)_2AgBiBr_6$, $Cs_2(Ag_{1-2x}\square_x Zn_x)BiBr_6$ and $Cs_2Ag(Bi_{1-x}Sb_x)Br_6$ based PV devices, with x = 10 at%.

Table 3
Fitting resistance (R) and constant phase element (Q) parameters obtained from EIS data measured on $Cs_2AgBiBr_6$, $(Cs_{1-x}Rb_x)_2AgBiBr_6$, $Cs_2(Ag_{1-2x}\square_x\ Zn_x)BiBr_6$ and $Cs_2Ag(Bi_{1-x}Sb_x)Br_6$ devices, with x = 10 at%.

	PCE (%)	R_1 [Ω]	Q_2 [10^{-3} F. s^{a-1}]	a	R_2 [Ω]	Q_3 [10^{-6} F.s^{b-1}]	b	R_3 [Ω]
Reference	1.6 %	10	$0.381.10^{-6}$	0.751	200	0.702	0.793	400
Rb	1.1 %	10	$0.455.10^{-6}$	0.867	300	0.795	0.868	826
Zn	0.4 %	10	$0.894.10^{-6}$	0.945	300	1.797	0.792	1566
Sb	0.3 %	10	$1.403.10^{-6}$	0.869	330	3.11	0.766	1785

Table 4
Calculated τ_1, τ_2, and $\tau_{average}$ values (see Supporting Information) for $Cs_2AgBiBr_6$,$(Cs_{1-x}Rb_x)_2AgBiBr_6$, $Cs_2(Ag_{1-2x}\square_xZn_x)BiBr_6$, and $Cs_2Ag(Bi_{1-x}Sb_x)Br_6$ thin films, with x = 10 at%, from TRMC measurements recorded upon pulsed laser excitation (λ = 420 nm) at room temperature.

λ= 420 (nm)	τ_1 (s)	τ_2 (s)	$\tau_{average}$ (ns)
Ref	1.7E−07	4.6E−09	4.8
Rb	5.5E−09	1.5E−07	6
Zn	1.8E−07	1.00E−08	14
Sb	1.4E−07	7.70E−09	9.78

2.32 eV). However, a longer charge lifetime could be expected for Sb doping in comparison with Zn one, due to the lower band gap. It is therefore speculated that Zn-substituted samples could induce electron trapping in the vacancies created by the substitution of a monovalent cation (Ag^+) by a divalent (Zn^{2+}) one (see previous Raman analysis), favoring the electron-hole separation and increasing their lifetime.

A narrow band gap and a larger charge carrier lifetime is expected to improve PCE. However, the PCE results (from J-V curves, Fig. 7 and Table 2) contrast with the evolution of both charge carrier lifetimes (from TRMC, Figure S5 and Table 4) and the electronic properties (from EIS, Fig. 8 and Table 3). For this reason, ultraviolet photoelectron spectroscopy (UPS) is exploited to determine the position of valence energy levels (Figure S6), aiming at correlating them with the decreasing of the PCE values [40–43].

The valence band energy (E_V) is determined from E_F and $E_{F\text{-}V}$ (see Supporting Information). The energy level of the conduction band is calculated from the measured optical band gap values for the reference and for the 10 at%-Rb, Zn and Sb substituted samples (2.32, 2.28, 2.26, and 2.20 eV, respectively), obtained from UV–VIS spectroscopy (Fig. 3). The energy diagrams accordingly drawn for all 4 samples are then shown in Fig. 9. Values obtained for the valence and conduction band energies of the $Cs_2AgBiBr_6$ reference sample match literature data [7, 40–43]. However, there are no previous measurements reported for Rb, Zn and Sb-substituted formulations.

The UPS measurements therefore show that in the case of reference and Rb-substituted samples (Fig. 9a and b), a suitably graded cascade of energy bands is obtained within the solar cell architecture, which consecutively promotes transport of electrons and holes within the device. On the other hand, for the Zn- and Sb-substituted samples (Fig. 9c and d), the conduction band of the photoactive material is of lower

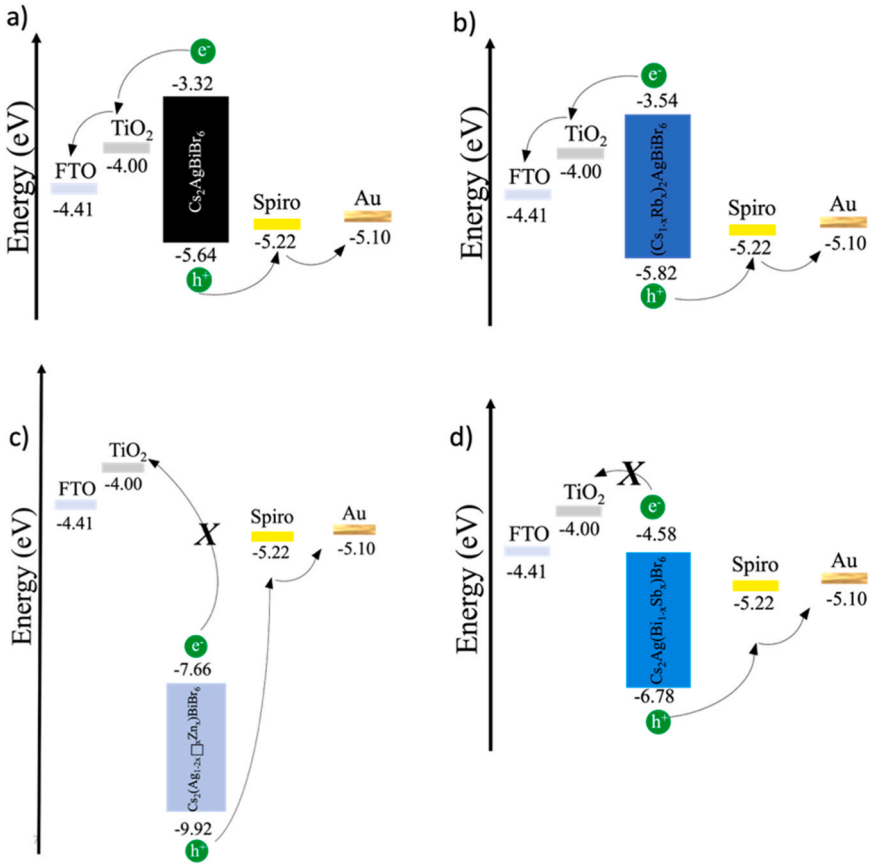

Fig. 9. Energy level diagrams of (a) $Cs_2AgBiBr_6$, (b) $(Cs_{1-x}Rb_x)_2AgBiBr_6$, (c) $Cs_2(Ag_{1-2x}\square_xZn_x)BiBr_6$, and (d) $Cs_2Ag(Bi_{1-x}Sb_x)Br_6$ PV devices architectures, with x = 10 at%.

energy level than the TiO_2 ETL. This shift impedes the transfer of electrons from the photoactive material to the ETL, which explains the (much) lower values of J_{sc} and PCE obtained with these samples. The energy level values used for FTO, TiO_2, Spiro-OMeTAD and Au in Fig. 9 are taken from the literature [44,45].

3.3. Effect of the substitution on the double perovskite lattice

At this stage, it appears crucial to correlate the experimental characterizations of the thin films and devices, described above, with a theoretical investigation of the structural changes potentially induced by the cationic substitution introduced in the $Cs_2AgBiBr_6$ double perovskite crystal lattice.

Very generally, the stable crystalline phase of $Cs_2AgBiBr_6$ belongs to the Fm3m cubic space group, which consists of alternating corner-sharing $AgBr_6$ and $BiBr_6$ octahedrons forming an ordered 3D pattern, with Cs in the center of the cavities (Fig. 10a). First-principles

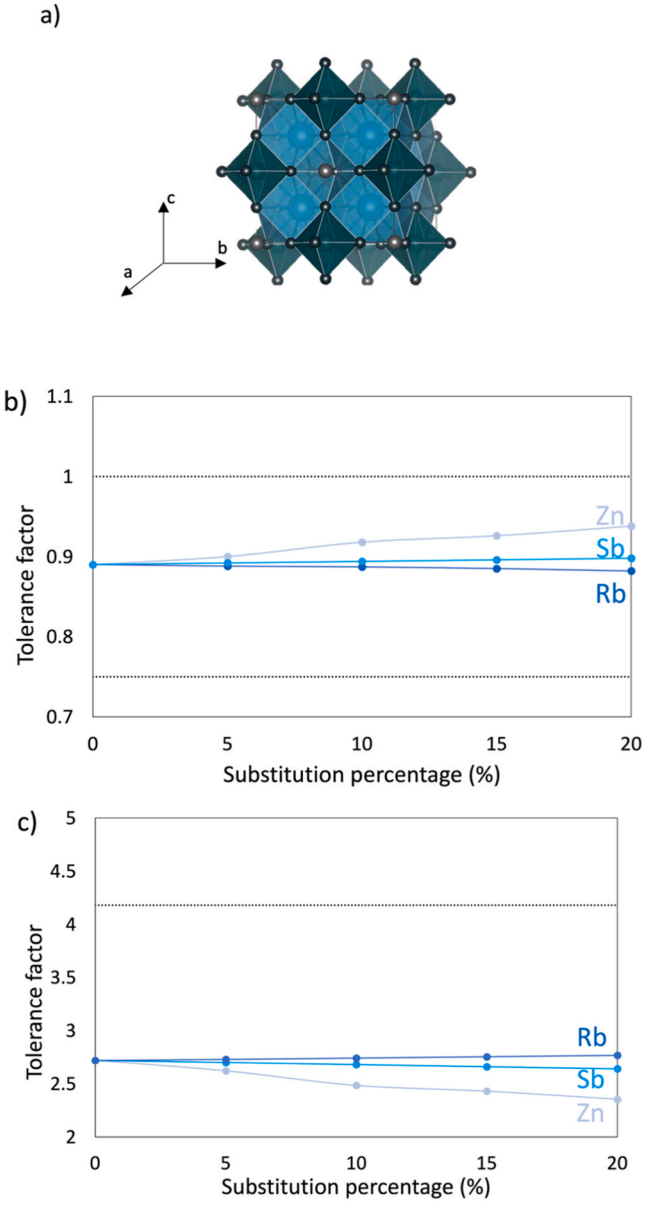

Fig. 10. (a) 3D representation of the crystal structure of the double perovskite; (b)Goldschmidt tolerance factor and (c) Bartel tolerance factor calculated for $Cs_2AgBiBr_6$,$(Cs_{1-x}Rb_x)_2AgBiBr_6$, $Cs_2(Ag_{1-2x}\square_xZn_x)BiBr6$, and $Cs2Ag(Bi_{1-x}Sb_x)Br6$, with x = 5, 10, 15 and 20 at%.

calculations show that the large band gap typically observed for $Cs_2AgBiBr_6$ exists due to this highly ordered structure. However, the distortion/tilting of octahedrons can have a significant effect on the electronic structure and consequently on the optoelectronic properties of the double perovskite compounds, including band gap, defects, carrier mobility, and can therefore be used to manipulate light absorption, as shown above [4].

Perovskite and double perovskite structures are usually expected to allow numerous cationic (or anionic) substitutions with very little impact on their structural stability.

The Goldschmidt tolerance factor, *t*, is often used to determine the stability of perovskite-like ABO_3 structure, as an evaluation tool of the mismatch between the different constitutive layers of the structure. It is calculated from the ionic radii of the atoms involved in the structure. An ideal cubic structure is obtained with a tolerance factor *t* close to unity.

The tolerance factor (*t*) is defined in Eq. 2:

$$t = \frac{r_A + r_O}{\sqrt{2} \times (r_B + r_O)} \quad (2)$$

where:

r_A is the ionic radius of the A cation (Cs);

r_B is the ionic radius of the B cation (Ag and Bi);

r_O is the ionic radius of the O anion (Br).

This value predicts whether a given ion can substitute for another ion on a particular crystal lattice site in the perovskite-like structure, without inducing any distortion. A stable structure requires a tolerance factor between 0.75 and 1 [46–48].

As $Cs_2AgBiBr_6$ compound features an $A_2BB'X_6$ double perovskite structure that can be assimilated to two ABX_3 lattices, the Goldsmith's tolerance factor is applied as a first approximation to this formulation in order to assess its stability during cationic substitution. Calculations are made for the four presently-considered compounds, using the Shannon ionic radii, which take into account the coordination numbers of the cations [19].

Fig. 10**a** shows the evolution of the calculated Goldschmidt tolerance factor for Rb, Sb, and Zn-substituted $Cs_2AgBiBr_6$ double perovskite compounds, as a function of the substitution rate. The values obtained for all substitution rates match the requirements for stability.

In addition to the above, it should be pointed out that *almost all* known perovskites have *t* values between 0.75 and 1.0. However, some perovskite structures were found to be unstable within the favorable *t* range of 0.8–0.9 [47]. The Goldschmidt tolerance factor may therefore present some limitations for determining the effect of a cationic substitution on the structural stability of the $Cs_2AgBiBr_6$ compound, especially considering its $A_2BB'X_6$ structure.

Therefore, for a better understanding of the $Cs_2AgBiBr_6$ structure stability, an alternative tolerance factor, *t'*, (Eq. 3) has been proposed by Bartel *et al.*, more suitably predicting structural stability for perovskite and double perovskite materials containing heavier halides, as in $Cs_2AgBiBr_6$ [49].

$$t' = \frac{r_X}{r_B} - n_A\left(n_A - \frac{r_A/r_B}{\ln\left(\frac{r_A}{r_B}\right)}\right) \quad (3)$$

where:

r_A is the ionic radius of the A-site (Cs);

r_B is the ionic radius of B-site (Ag and Bi);

r_X is the ionic radius of the halide (Br);

n_A is the oxidation state of A.

Their algorithm selects the optimal value as $t' = 4.18$ through the analysis of $\sim 3 \times 10^9$ candidate descriptors, so to define the decision limit for classification as (double) perovskite or non-perovskite material. The tolerance factors *t'* calculated for all presently-considered substitution rates satisfy the stability criteria (*i.e.*, below 4.18) required for the double perovskite structure (Fig. 10b).

However, in the $Cs_2AgBiBr_6$ compound, the B-sites are mainly occupied by two to three cations with different ionic radii, which means that a mean value of B-site ions radii has to be used for the calculation, which is known to not reflect the real situation of the double perovskite structure. The tolerance factors, *t* and *t'*, should therefore be used with caution, in order to obtain robust information about the crystal structural stability for B-sites substituted double perovskite compounds (which is the case for the zinc and antimony substitution).

To improve the reliability of structural stability predictions, one can also combine the tolerance factor *t'* with the octahedral factor μ, which is probably more appropriate for targeting the formability of the double perovskite structure, with respect to the local stability of the octahedrons for B-site substitution. For halide perovskites, the octahedral factor μ ($= r_B/r_X$) should be in the range $0.44 < \mu < 0.90$ [50].

In our case, if we consider the ionic radii in octahedral coordination for Ag^+, Bi^{3+}, Sb^{3+}, and Zn^{2+}, equal to 1.15, 1.03, 0.76, and 0.74 Å, respectively (the ionic radius of Br^- is equal to 1.96 Å), the octahedral factor for $AgBr_6$ is equal to 0.59, for $BiBr_6$ to 0.53, for $SbBr_6$ to 0.39, and for $ZnBr_6$ to 0.38.

$AgBr_6$ and $BiBr_6$ octahedrons are thus stable, but $SbBr_6$ and $ZnBr_6$ are not matching the stable range to form the double perovskite compound. We can thus conclude that Sb^{3+} and Zn^{2+} substitution in $Cs_2AgBiBr_6$ is not favorable based on these crystal structure considerations, and would destabilize the $Cs_2AgBiBr_6$ structure. Moreover, for the Zn^{2+} substitution, the charge neutrality condition is not preserved introducing cationic vacancies at the B-sites, which should also be considered in the instability of the crystal structure. By such local distortions on the octahedral sites, a phase change can occur, transforming the $Cs_2AgBiBr_6$ structure into a non-stoichiometric $Cs_3Bi_2Br_9$ structure (as observed experimentally from Raman spectroscopy, Fig. 6). This has been showed to induce strong localization of electron-hole pairs and a wide band gap, rendering $Cs_3Bi_2Br_9$ not suitable for optoelectronic applications [51]. In $Cs_3Bi_2Br_9$, the Bi atoms partially occupy Br_6 spaces in an ordered arrangement, leading to a vacancy-ordered double layer structure, which leads to distorted $BiBr_6$ octahedrons [51]. When Ag is incorporated in the structure to form the $Cs_2AgBiBr_6$ compound, the empty octahedral sites in $Cs_3Bi_2Br_9$ become occupied, and Ag and Bi are alternatively distributed into the crystal lattice. The incorporation of silver therefore leads to the elimination of the structural distortion in the $BiBr_6$ octahedrons.

The theoretical calculations of tolerance and octahedral factors conducted above rationalize the nature and degree of structural instability introduced into the $Cs_2AgBiBr_6$-based crystal lattices by the different cation substituents, notably in terms of the level of distortion occurring in their constitutive $(Bi/Ag)Br_6$ octahedrons. These structural perturbations, which are particularly significant in the case of Zn- and Sb-substituted formulations (substitution in B-site), clearly have a detrimental impact on the occurrence and efficiency of the electronic phenomena for the collection and transport of the photogenerated charges in the assembled PV devices, as established in particular by the J-V (see Fig. 7 and Table 2) and UPS measurements (Fig. 9 and Figure S6). These effects must therefore be considered with high significance, as they obviously counterbalance the benefits provided by the cationic substitution strategy in terms of increased light absorption (as determined by UV–VIS and PL measurements, Fig. 3 and Fig. 4) and longer carrier lifetimes (as determined by TRMC measurements, Table 4 and Figure S5).

4. Conclusions

This study provides new insights into the effects of cationic substitution in double perovskite compounds, such as $Cs_2AgBiBr_6$. The findings are crucial as they explain why reduced photovoltaic performances are obtained for these materials, despite their theoretical potential. Indeed, the results show that 10 at%-substituted formulations achieve an improved absorption and reduced band gap, while maintaining high quality of film morphology and thickness comparable to undoped $Cs_2AgBiBr_6$ benchmark. Further exploiting and discussing Raman, XPS, and structural analyses, the study confirms the successful incorporation of substituents, while revealing critical structural changes as distortions in the crystal lattice, with the specific creation of cationic vacancies in the case of a monovalent Ag^+ being substituted with a divalent Zn^{2+}. Finally, photovoltaic performance is shown to decline, as a result of shifts in valence and conduction bands (UPS) and of less efficient charge transfer mechanisms (EIS), with efficiencies of 1.1 % (Rb), 0.3 % (Zn), and 0.4 % (Sb), compared to 1.6 % for the reference. The combined use of complementary, advanced techniques such as PL, QFLS, EIS, TRMC, and UPS, enables to further qualify and quantify the disruptions occurring in terms of charge transport, specifically rationalizing them with the structural transformations that occur in the crystal lattice of the double perovskite formulations as a function of the nature and ratio of cationic dopant. Such correlations should be further investigated in future corresponding works, notably through theoretical investigations based on DFT calculations.

This work carries thus a dual focus on intrinsic material behavior and device implications, highlighting that cationic substitutions and the resulting modifications of the crystal lattice and electronic structure must be considered with caution, as the modification of the band gap and energy levels of the valence and conduction band can have a positive impact on light absorption as well as charge carrier mobility and lifetime, but be detrimental in terms of charge transfer between the different layers involved in the device stack due to a misalignment of their energy bands, leading to a drop in PV efficiencies. It therefore paves the way for future fundamental and applied studies. By unveiling the complex interplay between substitution mechanisms and functional performance, the present research provides a valuable roadmap for rationalizing the chemical design of $Cs_2AgBiBr_6$ double perovskite for PV applications. This will be achieved through a better understanding of their defects physics as well as their structural arrangements upon cationic and/or anionic substitution. Besides, band alignment between $Cs_2AgBiBr_6$ and ETL as well as HTL can also be optimized to increase further the PV performances of the devices [52]. These results contribute to the advancement of photovoltaic materials in the scientific community, opening new pathways for optimizing novel (substituted) compounds for solar cells applications, while providing insights for avoiding structural destabilization in future studies.

Declaration of Competing Interest

The authors declare that they have no known competing financial interests or personal relationships that could have appeared to influence the work reported in this paper.

Acknowledgments

This work is supported by the Department of Chemistry of the University of Liege. The authors also thank Prof. Luc Henrard and Dr. Rachel Gouttebaron from the University of Namur regarding both XPS and UPS measurements. The authors acknowledge fellow team members of GREEnMat for additional administrative, technical, and scientific support, especially Dr. Florian Gillissen.

Appendix A. Supporting information

Supplementary data associated with this article can be found in the online version at doi:10.1016/j.nxmate.2025.100655.

References

[1] M.T. Hörantner, T. Leijtens, M.E. Ziffer, G.E. Eperon, M.G. Christoforo, M. D. McGehee, H.J. Snaith, The potential of multijunction perovskite solar cells, ACS Energy Lett. 2 (10) (2017) 2506–2513.

[2] A.H. Slavney, T. Hu, A.M. Lindenberg, H.I. Karunadasa, A bismuth-halide double perovskite with long carrier recombination lifetime for photovoltaic applications, J. Am. Chem. Soc. 138 (7) (2016) 2138–2141.

[3] E. Greul, M.L. Petrus, A. Binek, P. Docampo, T. Bein, Highly stable, phase pure $Cs_2AgBiBr_6$ double perovskite thin films for optoelectronic applications, J. Mater. Chem. A Mater. 5 (37) (2017) 19972–19981.

[4] F. Schmitz, R. Bhatia, F. Lamberti, S. Meloni, T. Gatti, Heavy pnictogens-based perovskite-inspired materials: sustainable light-harvesters for indoor photovoltaics, APL Energy 1 (2023) 021502.

[5] N. Daem, J. Dewalque, F. Lang, A. Maho, G. Spronck, C. Henrist, P. Colson, S. D. Stranks, R. Cloots, Spray-coated lead-free $Cs_2AgBiBr_6$ double perovskite solar cells with high open-circuit voltage, Sol. RRL 5 (2021) 2100422.

[6] C.N. Savory, A. Walsh, D.O. Scanlon, Can Pb-free halide double perovskites support high-efficiency solar cells? ACS Energy Lett. 1 (5) (2016) 949–955.

[7] Z. Zhang, Q. Sun, Y. Lu, F. Lu, X. Mu, S.H. Wei, M. Sui, Hydrogenated $Cs_2AgBiBr_6$ for significantly improved efficiency of lead-free inorganic double perovskite solar cell, Nat. Commun. 13 (1) (2022) 1–12.

[8] P. Sebastiá-Luna, J. Calbo, N. Albiach-Sebastián, M. Sessolo, F. Palazón, E. Ortí, H. J. Bolink, Tuning the optical absorption of Sn-, Ge-, and Zn-substituted $Cs_2AgBiBr_6$ double perovskites: structural and electronic effects, Chem. Mater. 33 (20) (2021) 8028–8035.

[9] M.N. Tran, I.J. Cleveland, E.S. Aydil, Reactive physical vapor deposition of Yb-doped lead-free double perovskite $Cs_2AgBiBr_6$ with 95% photoluminescence quantum yield, ACS Appl. Electron Mater. 4 (9) (2022) 4588–4594.

[10] N. Pai, J. Lu, M. Wang, A.S.R. Chesman, A. Seeber, P.V. Cherepanov, D. C. Senevirathna, T.R. Gengenbach, N.V. Medhekar, P.C. Andrews, U. Bach, A. N. Simonov, Enhancement of the intrinsic light harvesting capacity of $Cs_2AgBiBr_6$ double perovskite: via modification with sulphide, J. Mater. Chem. A Mater. 8 (4) (2020) 2008–2020.

[11] L. Schade, S. Mahesh, G. Volonakis, M. Zacharias, B. Wenger, F. Schmidt, S. V. Kesava, D. Prabhakaran, M. Abdi-Jalebi, M. Lenz, F. Giustino, G. Longo, P. G. Radaelli, H.J. Snaith, Crystallographic, optical, and electronic properties of the $Cs_2AgBi_{1-x}In_xBr_6$ double perovskite: understanding the fundamental photovoltaic efficiency challenges, ACS Energy Lett. 6 (3) (2021) 1073–1081.

[12] M.S. Shadabroo, H. Abdizadeh, M.R. Golobostanfard, Elpasolite structures based on A_2AgBiX_6 (A: MA, Cs, X: I, Br): application in double perovskite solar cells, Mater. Sci. Semicond. Process 125 (2021) 105639.

[13] X. Yang, A. Xie, H. Xiang, W. Wang, R. Ran, W. Zhou, Z. Shao, First investigation of additive engineering for highly efficient $Cs_2AgBiBr_6$-based lead-free inorganic perovskite solar cells, Appl. Phys. Rev. 8 (4) (2021) 041402.

[14] F. Ji, Y. Huang, F. Wang, L. Kobera, F. Xie, J. Klarbring, S. Abbrent, J. Brus, C. Yin, S.I. Simak, I.A. Abrikosov, I.A. Buyanova, W.M. Chen, F. Gao, Near-infrared light-responsive Cu-doped $Cs_2AgBiBr_6$, Adv. Funct. Mater. 30 (2020) 2005521.

[15] Y. Liu, L. Zhang, M. Wang, Y. Zhong, M. Huang, Y. Long, H. Zhu, Bandgap-tunable double-perovskite thin films by solution processing, Mater. Today 28 (2019) 25–30.

[16] Y. Ou, Z. Lu, J. Lu, X. Zhong, P. Chen, L. Zhou, T. Chen, Boosting the stability and efficiency of $Cs_2AgBiBr_6$ perovskite solar cells via Zn doping, Opt. Mater. (Amst.) 129 (2022) 112452.

[17] H. Chen, C.R. Zhang, Z.J. Liu, J.J. Gong, M.L. Zhang, Y.Z. Wu, Y.H. Chen, H. S. Chen, Optoelectronic properties of Rb-doped inorganic double perovskite $Cs_2AgBiBr_6$, Chem. Phys. Lett. 771 (2021) 138501.

[18] Z. Zhang, C. Wu, D. Wang, G. Liu, Q. Zhang, W. Luo, X. Qi, X. Guo, Y. Zhang, Y. Lao, B. Qu, L. Xiao, Z. Chen, Improvement of $Cs_2AgBiBr_6$ double perovskite solar cell by rubidium doping, Org. Electron 74 (2019) 204–210.

[19] R.D. Shannon, Revised effective ionic radii and systematic studies of interatomic distances in halides and chalcogenides, Acta Crystallogr. Sect. A 32 (5) (1976) 751–767.

[20] E.M. Hutter, M.C. Gélvez-Rueda, D. Bartesaghi, F.C. Grozema, T.J. Savenije, Band-like charge transport in $Cs_2AgBiBr_6$ and mixed antimony–bismuth $Cs_2AgBi_{1-x}Sb_xBr_6$ halide double perovskites, ACS Omega 3 (9) (2018) 11655–11662.

[21] Y. Gao, K. Wang, M. Wang, J.I. Khan, A.H. Balawi, W. Liu, S. De Wolf, F. Laquai, Impact of cesium/rubidium incorporation on the photophysics of multiple-cation lead halide perovskites, Sol. RRL 4 (2020) 2000072.

[22] N. Singh, A. Agarwal, M. Agarwal, Performance evaluation of lead–free double-perovskite solar cell, Opt. Mater. 114 (2021) 1–11.

[23] Wu, C.; Zhang, Q.; Liu, Y.; Luo, W.; Guo, X.; Huang, Z.; Ting, H.; Sun, W.; Zhong, X.; Wei, S.; Wang, S.; Chen, Z.; Xiao, L. The Dawn of Lead-Free Perovskite Solar Cell: Highly Stable Double Perovskite $Cs_2AgBiBr_6$ Film. 2018, *1700759*, 2–9.

[24] L. Schade, S. Mahesh, G. Volonakis, M. Zacharias, B. Wenger, F. Schmidt, S. V. Kesava, D. Prabhakaran, M. Abdi-, Crystallographic, optical, and electronic properties of the $Cs_2AgBi_{1-x}In_xBr_6$ double perovskite: understanding the fundamental photovoltaic efficiency challenges, ACS Energy Lett. 6 (3) (2021) 1073–1081.

[25] A. Dey, A.F. Richter, T. Debnath, H. Huang, L. Polavarapu, J. Feldmann, Transfer of direct to indirect bound excitons by electron intervalley scattering in $Cs_2AgBiBr_6$ double perovskite nanocrystals, ACS Nano 14 (5) (2020) 5855–5861.

[26] S.J. Zelewski, J.M. Urban, A. Surrente, D.K. Maude, A. Kuc, L. Schade, R. D. Johnson, M. Dollmann, P.K. Nayak, H.J. Snaith, P. Radaelli, R. Kudrawiec, R. J. Nicholas, P. Plochocka, M. Baranowski, Revealing the nature of photoluminescence emission in the metal-halide double perovskite $Cs_2AgBiBr_6$, J. Mater. Chem. C. Mater. 7 (27) (2019) 8350–8356.

[27] M. Pantaler, K.T. Cho, V. Queloz, I. Garcia Benito, C. Fettkenhauer, I. Anusca, M. K. Nazeeruddin, D.C. Lupascu, G. Grancini, Hysteresis-free lead-free double perovskite solar cells by interface engineering, ACS Energy Lett. (2018) 1–14.

[28] A.H. Slavney, L. Leppert, D. Bartesaghi, A. Gold-parker, M.F. Toney, T.J. Savenije, B. Neaton, H.I. Karunadasa, Defect-induced band-edge reconstruction of a bismuth-halide double perovskite for visible-light absorption, J. Am. Chem. Soc. 2 (2017) 3–6.

[29] L. Schade, S. Mahesh, G. Volonakis, M. Zacharias, B. Wenger, F. Schmidt, S. Vajjala Kesava, D. Prabhakaran, M. AbdiJalebi, M. Lenz, F. Giustino, G. Longo, P. G. Radaelli, H.J. Snaith, ACS Energy Lett. 6 (2021) 1073.

[30] M.H. Engelhard, T.C. Droubay, Y. Du, X-Ray Photoelectron Spectroscopy Applications. Encyclopedia of Spectroscopy and Spectrometry, Elsevier, 2017, pp. 716–724.

[31] S. Yoon, B. Fett, A. Frebel, S. Kroisl, B. Herbig, M. Widenmeyer, B. Balke, G. Sextl, K. Mandel, A. Weidenkaff, Sb-Substituted $Cs_2AgBiBr_6$ —As Much As It Could Be?—Influence of Synthesis Methods on Sb-Substitution Level in $Cs_2AgBiBr_6$, Energy Technol. 10 (8) (2022) 2200197.

[32] Y. Bekenstein, J. Dahl, J. Huang, W.T. Osowiecki, J.K. Swabeck, E.M. Chan, P. Yang, P.Nano Alivisatos, The making and breaking of lead-free double perovskite nanocrystals of cesium silver–bismuth halide compositions, Letters 18 (6) (2018) 3502–3508.

[33] A. Maho, M. Lobet, N. Daem, P. Piron, G. Spronck, R. Cloots, P. Colson, C. Henrist, J. Dewalque, Photonic structuration of hybrid inverse-opal TiO_2 perovskite layers for enhanced light absorption in solar cells, ACS Appl. Energy Mater. 4 (2) (2021) 1108–1119.

[34] H.K. Adli, T. Harada, S. Nakanishi, S. Ikeda, Effects of $TiCl_4$ treatment on the structural and electrochemical properties of a porous TiO_2 layer in $CH_3NH_3PbI_3$ perovskite solar cells, Phys. Chem. Chem. Phys. 19 (39) (2017) 26898–26905.

[35] J. Li, W. Li, H. Dong, N. Li, X. Guo, L. Wang, Enhanced performance in hybrid perovskite solar cell by modification with spinel lithium Titanate, J. Mater. Chem. A Mater. 3 (16) (2015) 8882–8889.

[36] E.J. Juarez-Perez, M. Wuβler, F. Fabregat-Santiago, K. Lakus-Wollny, E. Mankel, T. Mayer, W. Jaegermann, I. Mora-Sero, Role of the selective contacts in the performance of lead halide perovskite solar cells, J. Phys. Chem. Lett. 5 (4) (2014) 680–685.

[37] M. Knezevic, V.D. Quach, I. Lampre, M. Erard, P. Pernot, D. Berardan, C. Colbeau-Justin, M.N. Ghazzal, Adjusting the band gap of $CsPbBr_{3-y}X_y$ (X = Cl, I) for optimal interfacial charge transfer and enhanced photocatalytic hydrogen generation, J. Mater. Chem. A 11 (12) (2023) 6226–6236.

[38] D. Bartesaghi, A.H. Slavney, M.C. Gélvez-Rueda, B.A. Connor, F.C. Grozema, H. I. Karunadasa, T.J. Savenije, Charge carrier dynamics in $Cs_2AgBiBr_6$ double perovskite, J. Phys. Chem. C. 122 (9) (2018) 4809–4816.

[39] B. Mohanty, J. Nayak, Band gap narrowing and prolongation of carrier lifetime in solution-processed CeO_2/CdS thin films for application as photoanodes in quantum dot sensitized solar cells, Ceram. Int. 47 (18) (2021) 26144–26156.

[40] A. Mohandes, M. Moradi, H. Nadgaran, Numerical simulation of inorganic $Cs_2AgBiBr_6$ as a lead-free perovskite using device simulation SCAPS-1D, Opt. Quantum Electron 53 (6) (2021) 319.

[41] Z. Li, S.R. Kavanagh, M. Napari, R.G. Palgrave, M. Abdi-Jalebi, Z. Andaji-Garmaroudi, D.W. Davies, M. Laitinen, J. Julin, M.A. Isaacs, R.H. Friend, D. O. Scanlon, A. Walsh, R.L.Z. Hoye, Bandgap lowering in mixed alloys of $Cs_2Ag(Sb_xBi_{1-x})Br_6$ double perovskite thin films, J. Mater. Chem. A Mater. 8 (41) (2020) 21780–21788.

[42] T.I. Alanazi, Design and device numerical analysis of lead-free $Cs_2AgBiBr_6$ double perovskite solar cell, Crystals 13 (2) (2023) 267.

[43] T. Luo, Y. Zhang, X. Chang, J. Fang, T. Niu, J. Lu, Y. Fan, Z. Ding, K. Zhao, S. (Frank) Liu, Dual interfacial engineering for efficient $Cs_2AgBiBr_6$ based solar cells, J. Energy Chem. 53 (2021) 372–378.

[44] X. Yang, W. Wang, R. Ran, W. Zhou, Z. Shao, Recent advances in $Cs_2AgBiBr_6$ -based halide double perovskites as lead-free and inorganic light absorbers for perovskite solar cells, Energy Fuels 34 (9) (2020) 10513–10528.

[45] M. Abdi-Jalebi, M.I. Dar, S.P. Senanayak, A. Sadhanala, Z. Andaji-Garmaroudi, L. M. Pazos-Outón, J.M. Richter, A.J. Pearson, H. Sirringhaus, M. Grätzel, R. H. Friend, Charge extraction via graded doping of hole transport layers gives highly luminescent and stable metal halide perovskite devices, Sci. Adv. 5 (2) (2019) 1–10.

[46] F. Bella, G. Griffini, J.P. Correa-Baena, G. Saracco, M. Grätzel, A. Hagfeldt, S. Turri, C. Gerbaldi, Improving efficiency and stability of perovskite solar cells with photocurable fluoropolymers, Science (1979) 354 (6309) (2016) 203–206.

[47] H. Wu, A. Erbing, M.B. Johansson, J. Wang, C. Kamal, M. Odelius, E.M. J. Johansson, Mixed-halide double perovskite Cs_2AgBiX_6 (X=Br, I) with tunable optical properties via anion exchange, ChemSusChem 14 (20) (2021) 4507–4515.

[48] Y. Jiao, S. Zhang, Z. Yang, G. Lu, Indirect-to-direct band gap transition and optical properties of metal alloying of $Cs_2AgM_xBr_6$ (M = Bi, In, Sb): insights from the first principles, Comput. Theor. Chem. 1148 (2019) 55–59.

[49] C.J. Bartel, C. Sutton, B.R. Goldsmith, R. Ouyang, C.B. Musgrave, L.M. Ghiringhelli, M. Scheffler, New tolerance factor to predict the stability of perovskite oxides and halides, Sci. Adv. 5 (2019) eaav0693.

[50] J.S. Manser, J.A. Christians, P.V. Kamat, Intriguing optoelectronic properties of metal halide perovskites, Chem. Rev. 116 (21) (2016) 12956–13008.

[51] M. Shi, G. Li, W. Tian, S. Jin, X. Tao, Y. Jiang, E.A. Pidko, R. Li, C. Li, Understanding the effect of crystalline structural transformation for lead-free inorganic halide perovskites, Adv. Mater. 32 (31) (2020) 2002137.

[52] N. Daem, J. Dewalque, D.K. Kim, G. Spronck, M. Attwood, J. Wade, C. Henrist, P. Colson, S. Heutz, R. Cloots, A. Maho, Improved photovoltaic performances of lead-free $Cs_2AgBiBr_6$ double perovskite solar cells incorporating tetracene as co-hole transport layer, Sol. RRL 7 (17) (2023) 2300391.